



ARCHIVIO ISTITUZIONALE DELLA RICERCA

Alma Mater Studiorum Università di Bologna Archivio istituzionale della ricerca

Orthogonal nanoarchitectonics of M13 phage for receptor targeted anticancer photodynamic therapy

This is the final peer-reviewed author's accepted manuscript (postprint) of the following publication:

Published Version:

Orthogonal nanoarchitectonics of M13 phage for receptor targeted anticancer photodynamic therapy / Ulfo, L; Cantelli, A; Petrosino, A; Costantini, PE; Nigro, M; Starinieri, F; Turrini, E; Zadran, SK; Zuccheri, G; Saporetti, R; Di Giosia, M; Danielli, A; Calvaresi, M. - In: NANOSCALE. - ISSN 2040-3364. - STAMPA. - 14:3(2022), pp. 632-641. [10.1039/d1nr06053h]

This version is available at: <https://hdl.handle.net/11585/847649> since: 2024-05-14

Published:

DOI: <http://doi.org/10.1039/d1nr06053h>

Terms of use:

Some rights reserved. The terms and conditions for the reuse of this version of the manuscript are specified in the publishing policy. For all terms of use and more information see the publisher's website.

(Article begins on next page)

This item was downloaded from IRIS Università di Bologna (<https://cris.unibo.it/>).
When citing, please refer to the published version.

This is the final peer-reviewed accepted manuscript of:

Ulfo L, Cantelli A, Petrosino A, Costantini PE, Nigro M, Starinieri F, Turrini E, Zadran SK, Zuccheri G, Saporetti R, Di Giosia M, Danielli A, Calvaresi M. Orthogonal nanoarchitectonics of M13 phage for receptor targeted anticancer photodynamic therapy. Nanoscale. 2022 Jan 20;14(3):632-641. doi: 10.1039/d1nr06053h. PMID: 34792088.

The final published version is available online at:
<https://doi.org/10.1039/d1nr06053h>

Terms of use:

Some rights reserved. The terms and conditions for the reuse of this version of the manuscript are specified in the publishing policy. For all terms of use and more information see the publisher's website.

This item was downloaded from IRIS Università di Bologna (<https://cris.unibo.it/>)

When citing, please refer to the published version.

ARTICLE

Received 00th January 20xx,
Accepted 00th January 20xx

DOI: 10.1039/x0xx00000x

Orthogonal Nanoarchitectonics of M13 Phage for Receptor Targeted Anticancer Photodynamic Therapy

Luca Ulfo,^{a,†} Andrea Cantelli,^{b,†} Annapaola Petrosino,^a Paolo Emidio Costantini,^a Michela Nigro,^a Francesco Starinieri,^a Eleonora Turrini,^c Suleman Khan Zadran,^a Giampaolo Zuccheri,^a Roberto Saporetti,^b Matteo Di Giosia,^b Alberto Danielli^{*a} and Matteo Calvaresi^{*b}

Photodynamic therapy (PDT) represents a promising therapeutic modality for cancer. Here we used an orthogonal nanoarchitectonics approach (genetic/chemical) to engineer M13 bacteriophages as targeted vectors for efficient photodynamic killing of cancer cells. M13 was genetically refactored to display on the phage tip a peptide (SYPIPD_T) able to bind the epidermal growth factor receptor (EGFR). The refactored M13_{EGFR} phages demonstrated EGFR-targeted tropism and were internalized by A431 cancer cells, that overexpress EGFR. Using an orthogonal approach to the genetic display, M13_{EGFR} phages were then chemically modified, conjugating hundreds of Rose Bengal (RB) photosensitizing molecules on the capsid surface, without affecting the selective recognition of the SYPIPD_T peptides. Upon internalization, the M13_{EGFR}-RB derivatives generated intracellularly reactive oxygen species, activated by an ultralow intensity white light irradiation. The killing activity of cancer cells is observed at picomolar concentrations of the M13_{EGFR} phage.

1. Introduction

Photodynamic therapy (PDT) is a minimally invasive therapeutic modality approved for clinical treatment of several types of cancer.^{1,2} In PDT, a compound with photosensitizing properties (photosensitizer, PS) upon activation by light, generates reactive oxygen species (ROS), responsible for cytotoxicity in neoplastic cells.^{1,2} The success of PDT is usually limited by the lack of selective accumulation of the PS at cancer cells, resulting in unwanted phototoxicity. Many strategies were devised to develop targeted photodynamic therapy.^{1,2} The “gold standard” is represented by the conjugation of PS with targeting agents such as monoclonal antibodies (mAb).³ This approach is very efficient, but still show some limitations related to i) the high cost of mAb, ii) the limited number of PS molecules conjugable to the mAb and iii) the reduction of mAb affinity for its target after chemical conjugation.⁴

Bacteriophages (phages) are ubiquitous viruses that infect bacteria but are inactive against eukaryotic cells. They are biocompatible, very uniform in size and morphology, and relatively stable at a high temperature, in a wide range of pH, and in the presence of nucleases and proteases.

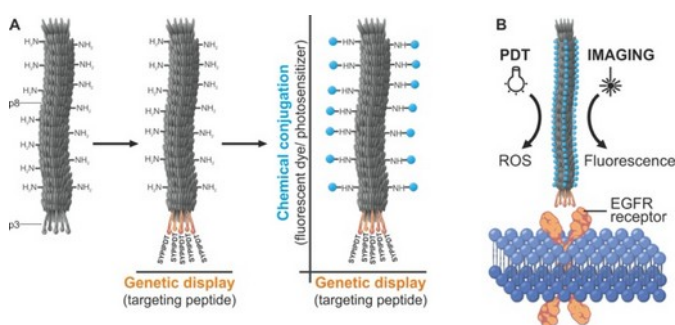
Scheme 1. A) Orthogonal engineering of M13 Phage. M13 phages with targeted tropism against EGFR receptor were generated through specific display on the minor coat protein pIII of SYPIPDT peptides. The SYPIPDT peptide does not contain any amino groups that may interfere with the orthogonal functionalization of the virus capsid, that involves amino groups on pVIII for selective chemical conjugation. B) EGFR targeted anticancer photodynamic therapy and imaging with M13_{EGFR} phage vector.

M13 phage have received growing attention as a well-defined protein-based platform for the assembly of nanostructured functional materials.⁵⁻¹⁹ Phages also represent innovative, harmless and effective delivery vectors, as they can undergo an extremely flexible genetic engineering allowing for a plethora of targeting designs.^{13,14,20-31} When compared to widely used drug delivery systems, they provide a high avidity for the target and a multitude of functionalization sites resulting in a high loading capacity and multivalency.³² In particular, the possibility to conjugate phages with suitable sensitizers conferring photokilling activity makes them interesting vectors for PDT applications.³³⁻⁴⁰ Filamentous phages, such as M13 can be pictured as a biological vehicle, 1000 nm long and 5 nm wide. The major coat proteins (pVIII, ~2700 copies) compose the side wall of the phage while four other minor coat proteins (called pIII, pVI, pVII, pIX, about 5 copies each) constitute the two distal ends.⁴¹ Here, we developed an orthogonal strategy⁴² to use recombinant phages as a robust and flexible platform for EGFR-targeted PDT approaches.

2. Experimental methods

Phagemid cloning and phage preparation.

The nucleotide sequence coding for the SYPIPDT peptide, targeting the EGFR receptor, was obtained by annealing oligonucleotides AD0127 (CATGGCCAGCTATCCGATTCCGGATAC CGGTGGCGGTG) and AD0218 (GATCCACCGCCACCGGTATCCGG AATCGGATAGCTGGC), generating NcoI and BamHI overhangs, respectively at the 5' and 3' of the coding sequence. This insert was cloned into a pSEX81 vector (ProGen) digested with NcoI and BamHI, generating the pPK15 phagemid. After ligation and transformation in *E. coli* (TG1), positive clones were identified by BspEI restriction digest and further validated by Sanger sequencing of the purified phagemid DNA. Ampicillin-resistant *E. coli* clones carrying the verified pPK15 phagemid were transduced with Hyperphage helper (ProGen) allowing for multivalent type 3 display of the SYPIPDT-pIII fusion on the phage tip (Figure S1). Bacteria were grown overnight in LB medium supplemented with Ampicillin (100 mg/L), Kanamycin (25 mg/L) and 0.4 mM IPTG in order to select for host cells



carrying the pPK15 phagemid and the helper phage, and to induce the expression of the SYPIPDT-pIII fusion protein from the P_{lac} promoter. The culture was pelleted for 30 min at 6000g to separate bacterial cells from the M13_{EGFR} (pPK15-derivative) phages present in the supernatant. PEG 8000 (4% w/v) and NaCl (3% w/v) were added to the phage supernatant. After stirring for 90 min at 4°C, the supernatant/PEG solution was centrifuged for 15 min at 15.000 g to precipitate the M13_{EGFR} virions. Pelleted phages were resuspended in milliQ water and precipitated by lowering the pH around the phage isoelectric point (IEP) with HCl.⁴³ After this IEP purification and precipitation step, phages were resuspended in 1xPBS pH7.2. This method proved efficient to remove the endotoxins deriving from the host bacterial cultures for downstream applications in cell culture experiments. Phage concentrations were inferred by measuring the absorbance at 269 nm wavelength in a UV-Vis spectrophotometer, using an extinction coefficient of $\epsilon = 3.84 \mu\text{M}$.

AFM analysis of M13_{EGFR}

AFM analysis was done on a Multimode 8 AFM (Bruker, U.S.A.) on specimens of fully hydrated phages adsorbed on the surface of freshly-cleaved muscovite mica (Electron Microscopy Sciences, U.S.A.). A small aliquot of a concentration-adjusted phage solution (in diluted PBS buffer) was layered on the surface of mica and let to absorb for 2 min. The AFM fluid cell

was then mounted and a small volume of ultrapure water (milliQ, Millipore, U.S.A.) was flowed in the cell. Imaging was performed in PeakForce Tapping® in liquid using ScanAsyst Fluid+ probes (Bruker, U.S.A.).

Image processing was performed using NanoScope Analysis software (ver. 1.80) by only flattening the micrographs. The (x,y,z) coordinates of the contour of several hundreds of individual phages were digitized semi-automatically from the micrographs using a custom-developed software developed in Matlab (Mathworks, U.S.A.). The measurement algorithm was derived from previously-developed procedures.^{44,45}

Bioconjugation and purification of M13_{EGFR} phages

Bioconjugation of RB. RB was dissolved in DMSO to obtain a concentration 10 mM, then 1-Ethyl-3-(3-dimethylaminopropyl) carbodiimide (EDC) and N-hydroxysuccinimide (NHS) were added under stirring, to obtain a final concentration of 10 mM and 15 mM, respectively. The solution was incubated for 3 hours at 25 °C under constant shaking at 700 rpm (ThermoMixer HC, S8012-0000; STARLAB, Hamburg, Germany) in dark conditions. 50 µl of the activated RB solution was then added dropwise under vigorous stirring, to 1 ml of a PBS solution containing M13_{EGFR} phages at a concentration 40 nM. The solution was then incubated overnight at 25 °C under mild stirring condition (700 rpm).

M13_{EGFR} labelling with FITC and TRITC. FITC was dissolved in DMSO to obtain a concentration 10 mM. 50 µl of the FITC solution was then added dropwise to 1 ml of a 100 mM sodium carbonate buffer (pH 9) solution containing M13_{EGFR} phages at a concentration 40 nM. The solution was then incubated overnight at 25 °C under continuous shaking (700 rpm). The same procedure was used for M13_{EGFR} labelling with TRITC.

Purification of the conjugated M13_{EGFR} phages. To remove unconjugated RB, TRITC, FITC and reaction coproducts, the M13_{EGFR} bioconjugates were purified via dialysis versus 100 mM sodium carbonate buffer (pH 9), using a regenerated cellulose membrane (14,000 kDa cut-off). UV-Vis spectra of the dialysate were performed at each step to monitor the purification process. The last dialysis cycle was performed against PBS 10 mM pH 7.4 in order to remove the alkaline buffer.

Immunoblotting

Protein extracts. A culture of E. coli TG1 transformed with pPk15 plasmid was grown to OD 0.4 in LB additionated with 2% of glucose. One mL of the culture was harvested to assess the expression of the non-induced pIII protein; the remaining culture was pelleted at 5000g for 5 minutes and resuspended in 5 mL of LB supplemented with 1 mM IPTG. The induced culture was incubated in shaking for 3 hours at 37 °C. Both samples (uninduced and induced) were resuspended in 1% SDS at equivalent OD 4.

Immunoblotting. Protein extracts and M13_{EGFR} purified phage at a concentration of 10¹⁰ pfu/µL were fractionated using a 12% (w/v) SDS gel and transferred to a PVDF membrane (Immobilion-P, Millipore, France). After treatment with blocking solution (5% milk in PBS pH 7.4 with 0.05% Tween),

the membrane was incubated with Anti-M13 pIII Monoclonal Antibody (BioLabs) diluted 1:5000 in blocking solution for 1h at room temperature. After three washes in PBS Tween 0.05%, the membrane was incubated with HRP-conjugated IGG anti-mouse secondary antibody diluted 1:10000 and incubated for 1h at room temperature. The membrane development was performed using ECL solution (1.25 mM luminol in Tris 100 mM pH 8.8; 6.8 mM coumaric acid; 30% H₂O₂). Images were acquired via ChemiDoc™ Imaging System (Bio-Rad).

Characterization of the M13_{EGFR} bioconjugates.

Absorption spectra were recorded using a Cary60 UV-Vis spectrophotometer (Agilent). The attenuated total reflectance Fourier transform infrared (ATR-FTIR) spectra were collected using Nicolet iS10 spectrometer. 10 µl of sample was deposited on the germanium crystal and let to dry slowly, producing a thin film. 70 scans were collected for each acquisition at 0.5 cm⁻¹ resolution. Omnic software was used for data collection and analysis.

Amplex® Red Assay.

The ability to generate peroxides, upon irradiation with visible light, was evaluated using the Amplex Red assay. Colorless, nonfluorescent Amplex Red, reacts with peroxides to form colored, fluorescent resorufin, catalyzed by HRP. The concentration of the produced peroxides is calculated as the difference of resorufin generated by irradiated samples and that of the non-irradiated references, i.e. identical solutions, kept in the dark. 10 µl of Amplex Red (AR) stock solution 50mM in DMSO was added to 1 ml of 50 mM phosphate buffer at pH 7.4 (PB) to obtain a final concentration of 500 µM. 10 µl of HRP 0.4 mg/ml in PBS were added to the AR solution, obtaining the final working solution (WS). The solutions (100 µl) under investigation, containing different concentrations (0 µM, 0.25 µM, 0.5 µM, 1 µM, 2.5 µM, 5 µM) of RB and M13_{EGFR}-RB in phosphate buffer 50 mM pH 7.4, were irradiated for 30 min with visible light (white LED Valex 30 W lamp, at 30 cm distance from the cell-plate, irradiation power density on the cell plate = 2.4 mW/cm²; measured with the photo-radiometer Delta Ohm LP 471 RAD). Three technical replicates were performed for each sample. After irradiation, WS (10 µL) was added to each well. The solutions were then incubated for 30 minutes at room temperature in dark conditions. After incubation, the emission was measured at 590 nm (λ_{ex} = 560 nm). A calibration curve generated using standard solutions of H₂O₂, was used to convert the fluorescence signal to the concentration of peroxides generated upon irradiation. Fluorescence measurements were carried using a Perkin Elmer EnSpire® Multimode Plate Reader.

Singlet Oxygen Assay.

We used as ¹O₂ detector 9,10-anthracenediyl-bis(methylene) dimalonate (ABMDMA). The disodium salt of ABMDMA reacts with ¹O₂ to give an endoperoxide. This reaction is detected by the bleaching of ABMDMA. From the decline of

the absorbance at 401 nm, the generation of $^1\text{O}_2$ upon irradiation is determined. Iso-absorbing solutions of RB and M13_{EGFR}-RB were prepared in deuterated PBS 10 mM pH 7.4. 500 μL of solutions containing a concentration 15 μM of RB and 25 μM of ABMDMA, maintained under vigorous stirring, were irradiated with a visible light lamp (Valex cold white LED, irradiance on the cuvette surface = 2.4 mW/cm², measured with the photo-radiometer Delta Ohm LP 471 RAD). The singlet oxygen quantum yield (Φ_{Δ}) was determined using Rose Bengal (RB) as the reference with a yield of 0.76 in PBS. The Φ_{Δ}^S of M13_{EGFR}-RB was calculated by the following equation $\Phi_{\Delta}^S = k_S/k_R \times \Phi_{\Delta}^R$ where k is the slope of the photodegradation rate of ABMDMA, S is the sample (M13_{EGFR}-RB), R is the reference (RB), and Φ_{Δ}^R is the Φ_{Δ} of the reference (RB).

Cell culture.

The A431 human epidermal carcinoma cell line was propagated in RPMI 1640 medium supplemented with 10% heat inactivated fetal bovine serum (FBS), 1% penicillin-streptomycin solution 100 U/mL and 1% L-glutamine 200 mM (Euroclone, Italy). Cells were grown at 37°C in a humidified incubator with 5% CO₂.

Validation of phage retargeting by flow cytometry.

Phage retargeting was determined by flow cytometry. All the flow cytometric analyses were performed on a BioRad S3e cell sorter. FITC-labeled phages (M13_{EGFR}-FITC) were incubated with A431 cells at a multiplicity of 100:1 for 30 min and the population was gated on forward and side scatter. FITC-related fluorescence was measured in the FL1 channel (excitation 488 nm, emission filter 525/30 nm). The median fold-increase fluorescence was used to quantify the numbers M13_{EGFR}-FITC targeted cells compared to controls. At least 10,000 events were evaluated for each analyzed sample. Data analysis was processed using FlowJo™.

Validation of phage retargeting by confocal microscopy.

M13_{EGFR} phages were labeled with TRITC and their interaction with A431 cells was inspected using a confocal microscopy (NIKON Eclipse Ti2). Round coverslips were placed on the bottom of a Corning 6-well plate, 2×10⁵ cells/well were seeded and grown overnight to 25% confluency. Afterward, cells were incubated for 90' with complete medium supplemented with M13_{EGFR}-TRITC at the final concentration of 1 μM . Cells were washed 3 times with PBS and then stained for 30' with green-fluorescent Calcein AM and Hoechst 33342 (Invitrogen) at the final concentration of 100 nM and 1 $\mu\text{g}/\text{mL}$, respectively. The round coverslips were removed from the 6-well plate, fitted into an Attofluor cell chamber (Invitrogen, USA) with 1 mL of DMEM without phenol red supplemented with 10 % FBS, 1 % Penicillin-Streptomycin and 1 % L-glutamine. Cell images were then acquired with a NIKON Eclipse Ti2 confocal microscope.

Immunocytochemistry.

To follow the retargeting of unconjugated phages, immunocytochemistry assays were carried out. 1×10⁶

cells/well were seeded and grown overnight to 25% confluency in adhesion on uncoated coverslips. Cells were then incubated for 45 minutes with complete medium supplemented with 2×10¹⁰ M13_{EGFR} or M13 phages. Afterwards medium was removed, and coverslips were washed thrice with PBS 1X, fixed with a 4% PFA solution for 15', permeabilized with Triton 0.1% for 15' and blocked with 2% low fat milk solution for 45'. Cells were then incubated with mouse anti-pVIII (1:300) antibody (ProGen) for 1h at RT, washed and incubated for 1h at RT with a goat anti-mouse IgG antibody (Invitrogen) conjugated with Alexa Flour®568 (dilution 1:1000). Cells were washed three times to remove excess antibody and stained with Hoechst 33342 (Invitrogen) at the final concentration of 1 $\mu\text{g}/\text{mL}$. Images were acquired with a NIKON Eclipse Ti2 confocal microscope and analyzed with ImageJ.

Photoactivity of M13_{EGFR}-RB phage monitored with SOSG.

The photodynamic activity of the RB-conjugated M13_{EGFR} phages was evaluated by monitoring the fluorescence of SOSG (singlet oxygen sensor green) with confocal microscope (NIKON Eclipse Ti2). SOSG is a detection reagent which emits green fluorescence at 525 nm in presence of singlet oxygen. A431 cells were seeded on round coverslips placed at the bottom of a 6-well plate. About 1 million cells per well were seeded and grown overnight at 37° with 5% CO₂. Afterward, cells were incubated for 90' with complete medium supplemented with PBS (control) or M13_{EGFR}-RB at the final concentration of 1 μM . Next, medium was removed and cells were washed 3 times with PBS, fixed with 4% paraformaldehyde (PFA) solution for 15' at room temperature and washed thrice with PBS. A solution 1 μM of SOSG (3% MeOH in water) was then added, incubated for 15' with the cells and washed thrice with PBS. The round coverslip was then mounted in the Attofluor cell chamber, covered with 1 ml of PBS and green fluorescence emission was monitored with a NIKON Eclipse Ti2 confocal microscope. Acquisitions were performed every 10' for 70' irradiating with white light between each measurement in LIGHT samples, white light was held off in acquisitions of DARK controls. Fluorescence intensity was quantified using ImageJ on acquired images. Results are expressed as the SOSG fluorescence mean \pm SD of at least four independent image quadrants.

Photodynamic killing of A431 cells (PDT).

About 20,000 cells/well were seeded in 96-well flat bottom plates (Corning) and incubated overnight to 90% confluency. Afterwards, cells were treated 90' with growth medium supplemented with Rose Bengal (RB), bare M13_{EGFR} or M13_{EGFR}-RB. Cells were washed twice with PBS, in order to remove free phage/photosensitizer, and then irradiated in PBS for 30' with a LED light determining a 2 mW/cm² irradiance on the plate surface. At the end of irradiation, PBS was removed, and cells were incubated in complete medium for 24 h at 37 °C with 5% CO₂. Control plates were treated the same but kept under dark conditions.

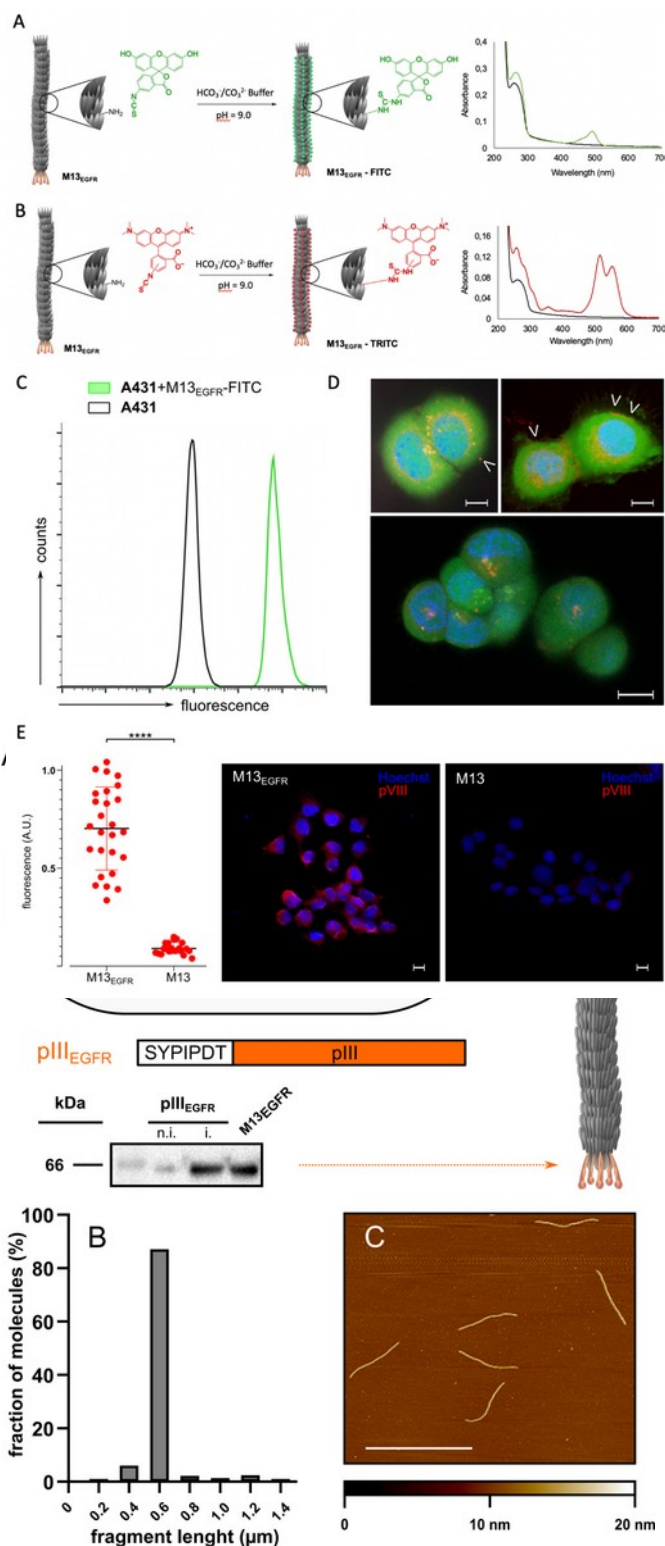
Cell viability and membrane polymerization assays.

Cell survival after PDT was tested using MTT assays. Briefly, culture medium was removed and replaced with fresh medium supplemented with MTT at the final concentration of 0.5 mg/mL, thus cells were incubated at 37°C with 5% CO₂ for 90'. MTT supplemented medium was then removed and replaced with DMSO for the formazan solubilization. Absorbance was then determined at 570 and 690 nm wavelength using EnSpire multimode plate reader (Perkin Elmer, USA). All results are expressed as the mean \pm SD of at least three independent experiments. To assess cell viability and membrane permeabilization in response to phage-mediated PDT, a live/dead Calcein/Propidium Iodide (PI) staining was implemented on the A431 cell-line. 1 million cells were seeded in each well of a 6-well plate containing 25 mm round coverslip at the bottom of each well and grown overnight to 50% confluency. Next, cells were incubated for 90' with complete medium supplemented with M13_{EGFR}-RB at the final concentration of 1 μ M, washed 3 times with PBS and then irradiated for 30' with a LED light as described above. Immediately after the treatment (t1) or 24 h after the treatment (t2) cells were stained for 15' with 100 nM Calcein AM and 30 nM PI, respectively. After the staining, the round coverslip was mounted in the cell chamber and images were acquired on a NIKON Eclipse Ti2 confocal microscope with appropriate filters.

3. Results and discussion

Fig. 1. Genetic engineering of M13_{EGFR} phage. A) Episomal elements encoding the M13_{EGFR} phage and immunoblotting of the SYPIPDT-pIII fusion, demonstrating incorporation in the purified virion. pPK15: *bla* ampicillin resistance cassette (red); ColE1 ori; pIIIEGFR fusion (orange). M13 Δ pIII helper: *aph* kanamycin resistance cassette (blue); p15A ori, M13 genes (except for pIII, dark grey). B) size distribution of the M13_{EGFR} phages as determined by AFM. C) AFM micrograph of purified M13_{EGFR} phages. Scale bar = 1 μ m.

M13 phages with targeted tropism against EGFR receptor (M13_{EGFR}) were generated through specific display on the minor coat protein pIII of SYPIPDT peptides.⁴⁶ Aberrant activity EGFR receptors can result in unregulated growth stimulation and tumorigenesis in various tumour types, including breast, lung, brain, head and neck, and colon tumours.⁴⁷ Given their role in tumorigenesis, various therapeutics targeting EGFR have been approved.⁴⁷ The development of drugs to specifically target EGFR has represented a paradigm shift in oncology from non-specific chemotherapy to a molecularly targeted approach.⁴⁷⁻⁵⁷ A synthetic oligonucleotide encoding the SYPIPDT peptide was cloned in frame with the pIII gene of a phagemid vector allowing for multivalent type 3 display on the phage tip using helper phages (Fig. 1A). The SYPIPDT peptide was selected because i) it has a known targeting activity to EGFR receptors and ii) it does not contain any amino groups that may interfere with the orthogonal functionalization of the virus capsid, that involves free amino groups of N-terminal alanine and lysine (Lys8) on pVIII for selective chemical conjugation.^{58,59} Because the recognition moiety is genetically displayed on the minor



coat protein (pIII), the 2700 copies of the major coat protein pVIII maintain a high cargo capacity (~5400 conjugating sites) to anchor imaging tags or PS to the vector capsid,^{42,60} without affecting the selective recognition of the SYPIPDT peptides. This represents a significant advantage over previous, non-orthogonal strategies involving refactored phage vectors for PDT.³⁶ The correct expression of the SYPIPDT-pIII fusion was checked by immunoblotting with an anti-pIII antibody. A band of the expected molecular weight was induced in *E. coli*

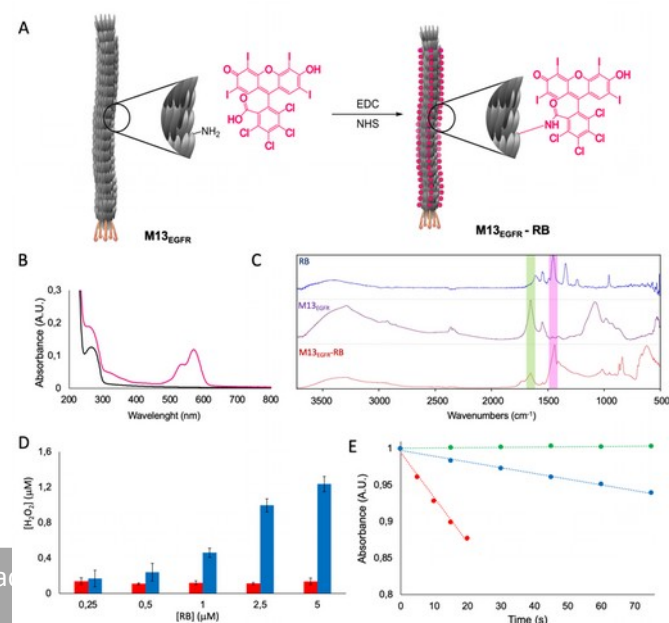
cultures carrying the pPK15 phagemid (Fig. 1A). The same SYIPDT-pIII fusion was also detected in the purified recombinant phages, demonstrating the incorporation of the targeting peptide in the M13_{EGFR} virions. These phage preparations were further characterized by Atomic Force Microscopy (AFM) in solution. Image analysis showed that M13_{EGFR} phages appear intact (with an apparent diameter of about 4.7 nm) and with a contour length distribution centered around 575 (± 45) nm (median \pm interquartile range, estimated over N=365 phage molecules) (Fig. 1B and 1C). The shortened phage length proves the correct packaging into the M13_{EGFR} virion of the smaller pPK15 phagemid, which is preferred over the packaging of the larger M13 Δ pIII helper phage genome. In fact, less than 7% of the measured phages appeared to have a significantly longer contour length than this population: most of these were about twice the average phage length, so they could presumably be dimeric molecules. Very few molecules displayed a contour length significantly longer than twice the average (see Figure 1B). The intact architecture and the expected size distribution (Fig. 1B and 1C), support the successful engineering of the M13_{EGFR} platform.

In order to monitor the ability of the displayed peptides to selectively target the refactored phages to A431 cells, M13_{EGFR} phages were chemically conjugated with FITC (Fig. 2A) and then characterized by flow cytometry. A431 are an epidermoid human squamous carcinoma cell line, characterized by amplification of the EGFR gene, expressing high levels of the receptors on their membranes. As such, the A431 represents a **Fig. 2.** A) Conjugation of FITC to M13_{EGFR}. Absorption spectra of M13_{EGFR} (black line) and M13_{EGFR}-FITC (green line). Considering the initial M13_{EGFR} concentration and the molar extinction coefficients of FITC, approximately 200 FITC molecules are conjugated to M13_{EGFR}. B) Conjugation of TRITC to M13_{EGFR}. Absorption spectra of M13_{EGFR} (black line) and M13_{EGFR}-TRITC (red line). Considering the initial M13_{EGFR} concentration and the molar extinction coefficients of TRITC, approximately 1700 TRITC molecules are conjugated to M13_{EGFR}. C) Flow cytometry analysis of refactored M13_{EGFR}-FITC phages targeting the EGFR-overexpressing A431 cell line. D) A431 confocal microscopy images of internalized intracellular M13_{EGFR}-TRITC phages (red); nuclei (Hoechst, blue); cytoplasm (calcein AM, green). Arrowheads highlight phages localized at the cell boundaries. E) Retargeting to the EGFR receptor promotes specific internalization of M13_{EGFR} phage vector. Immunostaining: pVIII major capsid protein (red), nuclei (Hoechst, blue). Scale bar = 10 μ m.

suitable cell line for testing the EGFR-retargeted phages recognition ability. The addition of M13_{EGFR}-FITC (multiplicity of 100:1) resulted in a clear shift of the fluorescence intensity of A431 cells, already after 30 min incubation, demonstrating the targeting of the phage vector (Fig. 2C). Filamentous phages displaying receptor-targeting peptides can be selectively internalized by cells, as shown for the SKBR-3 breast cancer line.⁶¹ To investigate the uptake of M13_{EGFR} and its cellular localization, a M13_{EGFR}-TRITC conjugate was produced (Fig. 2B). When co-incubated with A431 cells, M13_{EGFR}-TRITC showed

rapid internalization of the phage vector within 30 min, with intracellular accumulation in the perinuclear compartments of the cell (Fig. 2D). Careful inspection of the micrograph confocal plans allowed also to detect M13_{EGFR} phages at the cell surface (arrowheads Fig. 2D), arguing in favour of a receptor-mediated internalization of M13_{EGFR}. This is a desirable property for a PDT vector, since the photosensitizers need to be internalized for maximum efficacy of the treatment. The selective internalization of the M13_{EGFR} vector was further investigated in immunocytochemistry with antibodies specific for the major capsid protein pVIII (Fig. 2E). The display of the SYIPDT peptide fused to pIII elicited a >10-fold increase in the internalization rate of M13_{EGFR}, as compared to the parental non-retargeted M13 phage, demonstrating the modified tropism of the engineered phage vector.

Rose Bengal (RB) is an FDA-approved vital dye that has been used clinically for over 30 years in ophthalmology procedures.⁶² Under the trade name PV-10, rose bengal has been the subject of clinical trials for its efficacy in the treatment of human melanoma.⁶² It is currently in stage III trials.⁶² RB molecules are also commonly used as photosensitizers, with extremely interesting applications in PDT.⁶³ We conjugated RB molecules to the capsomers of M13_{EGFR}. The M13_{EGFR}-RB biconjugate was synthesized via EDC/NHS cross coupling reaction between the amino acid amine groups of M13_{EGFR} capsomers and the activated carboxylic-acid group of RB (Fig. 3A). The absorbance band of the purified M13_{EGFR}-RB (Fig. 3B) shifted to 560 nm and became broader following conjugation with M13_{EGFR}. These spectral changes confirmed that RB was attached to M13_{EGFR} capsid.⁶⁴ Considering the initial M13_{EGFR} concentration and the molar extinction coefficients of RB, approximately 710 RB molecules were conjugated to M13_{EGFR}. The ATR-FTIR spectra (Fig. 3C) also support the conjugation of RB to M13_{EGFR}. In fact, in the ATR-FTIR spectrum of the M13_{EGFR}-RB bioconjugate it is possible to recognize both the Amide I band (1652 cm⁻¹) typical of the phage⁴³ and one of the diagnostic bands of the RB (1439 cm⁻¹), corresponding to the C=C stretching of the aromatic moiety of the molecule.^{65,66} The ability of M13_{EGFR}-RB to generate ROS, upon irradiation with visible light, was evaluated using the Amplex Red assay to detect peroxides (Fig. 3D) and ABMDMA to detect ¹O₂ (Fig. 3E). M13_{EGFR}-RB showed an improved ability to generate peroxides compared to free RB. On the opposite, the singlet oxygen quantum yield (Φ_{Δ}) of M13_{EGFR}-RB ($\Phi_{\Delta}^{\text{M13-RB}}$ =



0.10) was reduced with respect to free Rose Bengal (RB) ($\Phi_{\text{A}}^{\text{RB}} = 0.76$).

Conjugation of RB to M13_{EGFR} capsomer proteins induces a photoactivation switch from type II (energy transfer process) to type I (electron transfer process) mechanisms, which increases the generation of peroxides over $^1\text{O}_2$, a phenomenon already observed when RB is conjugated to proteins.⁶⁷ In general, a sacrificial electron donor is required to activate the type I mechanism, so electron-rich environments favor type I mechanisms.⁶⁸ In this case, the protein residues of the phage could directly participate in the electron transfer process,

Fig. 3 A) Conjugation of RB to M13_{EGFR}. B) Absorption spectra of M13_{EGFR} (black line) and M13_{EGFR}-RB (rose line). C) ATR-FTIR spectra of RB, M13_{EGFR} and M13_{EGFR}-RB. D) Generation of peroxides using different concentrations of RB (red) and M13_{EGFR}-RB (blue). E) Determination of the generation of $^1\text{O}_2$ following the decrease of ABMDMA absorbance vs. irradiation time under white light irradiation for M13_{EGFR} (green line), M13_{EGFR}-RB (blue line) and RB (red line).

eliminating the need the external addition of electron donating species.^{69–72} This behavior is extremely interesting because fabrication of type I photosensitizer for anticancer PDT is an emerging topic.⁷³

To test the photodynamic performances of bioconjugated M13_{EGFR}-RB, we set out to monitor the *in cellulo* production of ROS during the irradiation with various reporters.⁷⁴ First attempts were carried out with AmplexRed and dichlorofluorescein (DHFC) to detect peroxides generated in the cell by irradiation of the M13_{EGFR}-RB vector. These experiments missed to provide conclusive evidence since the spectral properties of these dyes overlap those of the RB sensitizer, making it difficult to distinguish between the different contributions of the signal. Similarly, the use of CellROX™ detector proved inconclusive since the fluorescence of this ROS responsive dye was simply activated by cell irradiation (data not shown). On the opposite, the spectral properties of singlet oxygen sensor green (SOSG) can be easily distinguished from RB and it was not activated by the photodynamic irradiation alone, providing a convenient choice to demonstrate *in cellulo* production of ROS ($^1\text{O}_2$) mediated by the phage vector (Fig. 2). A431 cells were incubated with M13_{EGFR}-RB and SOSG for 90 min, and subsequently irradiated with a white LED lamp. Immediately after irradiation micrographs were taken at regular time intervals with a confocal microscope to follow SOSG emission.

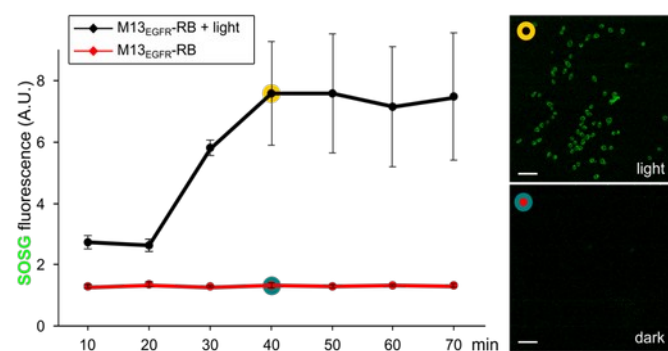


Fig. 4. Photoactivity of M13_{EGFR}-RB monitored with SOSG fluorescence during light irradiation. The fluorescence intensity of SOSG increases proportionally to the concentration of singlet oxygen, estimating the intracellular ROS produced. Scale bar = 50 μm .

SOSG fluorescence peaked and saturated after 40 minutes, only in irradiated specimens in the presence of M13_{EGFR}-RB. In control samples kept in the dark and in irradiated samples without M13_{EGFR}-RB, the fluorescent signal of SOSG was consistently weaker (Fig. 4). Recalling internalization and the improved ability of the engineered vector to generate peroxides over singlet oxygen, these results demonstrate that M13_{EGFR}-RB is a strong generator of intracellular ROS in response to light activation.

The M13_{EGFR}-RB bioconjugates were then tested for their anticancer photodynamic activity. A431 cells were incubated for 90 min with M13_{EGFR}-RB, M13-RB or with RB alone. After washing to remove free photosensitizing species, cells were irradiated for 30 min with a low irradiance (2.4 mW/cm²) white LED light. Controls were kept in the dark. After 24 hours recovery, survival rates were measured by a MTT cell viability assay. While M13-RB and RB alone did not promote any significant cytotoxic effect, M13_{EGFR}-RB proved very efficient in A431 killing, starting already from 100 nM RB equivalents, corresponding to 140 pM M13_{EGFR}-RB phage concentration (Fig. 5A), that to the best of our knowledge is one of the lowest concentrations ever observed for PDT treatment. At the highest concentration tested, M13_{EGFR}-RB provoked almost complete A431 killing, with membrane permeabilization and loss of cell viability, as evident from the dramatic decrease in calcein staining and the strong accumulation of the otherwise impermeant propidium iodide stain, already at 30 min post-irradiation (Fig. 5B). These effects do not occur in non-irradiated specimens (Figs. 5A) confirming the high tolerability and low cytotoxicity of M13 phages *per se* (absence of dark toxicity). The photodynamic killing of non-refactored phages (M13-RB, Fig 5C) proved less potent, and almost absent at lower concentrations of RB equivalents, confirming the selectivity conferred by the phage refactoring. Only at the higher phage concentrations of M13-RB, a non-specific killing effect was observed, likely mediated by traces of phages deposited passively onto the cell layer during the incubation. Collectively, these results indicate that M13_{EGFR}-RB mediates production of cytotoxic ROS upon internalization and the light-dependent activation of the RB photosensitizer.

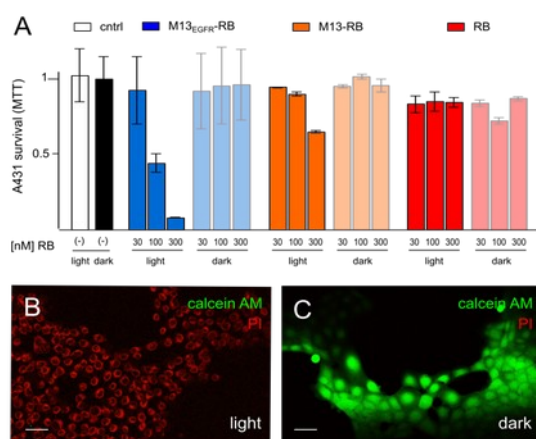


Fig. 5. Photodynamic killing of epidermoid cancer cell line. A) A431 survival rates 24h after low-intensity PDT treatment with M13_{EGFR}-RB or with RB alone; controls were kept in the dark; error bars = standard deviation of six replicates. B) M13_{EGFR}-RB induce (rapid) onset of membrane permeabilization and loss of cell viability, in response to light irradiation (30 min post-irradiation); calcein AM, green; PI, propidium iodide, red; scale bar 50 μm. C) same as B) without irradiation.

Conclusions

The developed orthogonal approach (genetic/chemical) to engineer M13 bacteriophages for receptor targeted (EGFR-targeted) PDT demonstrates that M13 can serve as potent vector platform for anticancer PDT: i) the phage tropism can be conveniently tweaked to target diverse receptors overexpressed in cancer cells ii) both therapeutic and imaging tags can be chemically conjugated to the phage capsid, without perturbing the recognition ability of the phage. iii) a palette of functional groups ready for the orthogonal chemical modification of the phage is available: amines (as showed in this work),^{58,75} aminoacids naturally present on the capsomer as aspartic and glutamic acid or tyrosine,^{58,75} or other natural (cysteine)^{58,75} and unnatural cross-linkable amino acid (i.e. L-azidohomoalanine, Aha)^{76–78} that can be easily incorporated in the pVIII capsid protein by mutagenesis.

If compared to other targeted therapies: i) phages represent flexible retargetable platforms for PDT, given the possibility to retarget the vector by genetic display of the targeting moiety. ii) targeting peptides identified in literature by phage display can be directly used, as they are stabilized by the fusion to the phage proteins, iii) phage production is cost-effective. Protocols for phage productions in bacterial cells allow to drop the cost to ~ 1 \$ per 10¹² PFU,⁷⁹ which is considered the standard dose for a phage treatment. By comparison, the production of therapeutic antibodies (Ab), the most used targeting molecules for PDT, is almost ten times more expensive.⁸⁰ iv) the pentavalent display of the targeting peptides on pIII allows to enhance their binding affinity/avidity; v) Ab conjugation with sensitizers is a cumbersome procedure, allowing a maximum multivalency of 5–10 sensitizers per molecule, which also often leads to

reduced Ab stability and/or affinity.⁴ On the contrary the M13 phage platform can be conjugated with hundreds/thousands of sensitizers without impinging upon the targeting moiety. Thereby, many more sensitizers can be delivered to the target per binding event as compared to one/few sensitizers for antibodies.

The use of natural phages conjugated with photosensitizers has been applied successfully to antimicrobial PDT in the past.³³ However, the orthogonal approach developed for M13 in this work presents several advantages over other applications of phages in PDT. In fact, differently from previous applications of phages for anticancer PDT, i) the targeting agent is expressed genetically and not chemically conjugated,³⁷ ii) the orthogonal design keeps the possible interference of conjugated molecules on the targeting moiety at minimal levels.³⁶ The nanoarchitectonic approach^{81,82} developed here represents a significant advantage for the translation of phages from bench-to-bedside, considering that several photosensitizers already approved for clinical applications or under clinical trials⁸³ and acting in the "diagnostic window", such as chlorines or cyanines, can be easily conjugated to the phage capsid.

Author Contributions

L.U., A.C., A.P., P.E.C., M.N., F.S., E.T., S.K.Z., G.Z., R.S. and M.D.G.: Investigation, Data Curation, Formal Analysis. A.D. and M. C.: Conceptualization, Formal Analysis, Funding acquisition, Methodology, Supervision. All authors: Writing.

Conflicts of interest

There are no conflicts to declare.

Funding and acknowledgements

M.D.G. was supported by a FIRC-AIRC fellowship for Italy (id. 22318). The research leading to these results has received funding from AIRC under MFAG 2019 - ID. 22894 project - P.I. - M.C. and from a Proof-of-Concept grant by the Italian Ministry of Economic Development and the University of Bologna to A.D.

Notes and references

- 1 D. E. J. G. J. Dolmans, D. Fukumura and R. K. Jain, *Nat. Rev. Cancer*, 2003, **3**, 380–387.
- 2 H. Shi and P. J. Sadler, *Br. J. Cancer*, 2020, **123**, 871–873.
- 3 M. Mitsunaga, M. Ogawa, N. Kosaka, L. T. Rosenblum, P. L. Choyke and H. Kobayashi, *Nat. Med.* 2011, **17**, 1685–1691
- 4 G. A. M. S. Van Dongen, G. W. M. Visser and M. B. Vrouenraets, *Adv. Drug Deliv. Rev.*, 2004, **56**, 31–52.
- 5 Y. S. Nam, H. Park, A. P. Magyar, D. S. Yun, T. S. Pollom and A. M. Belcher, *Nanoscale*, 2012, **4**, 3405–3409.
- 6 C. Kyu Jeong, I. Kim, K.-I. Park, M. Hwa Oh, H. Paik, G.-T.

- Hwang, K. No, Y. Sung Nam and K. Jae Lee, *ACS Nano*, 2013, **7**, 11016–11025.
- 7 P. Passaretti, Y. Sun, I. Khan, K. Chan, R. Sabo, H. White, T. R. Dafforn and P. G. Oppenheimer, *Nanoscale*, 2019, **11**, 13318–13329.
- 8 J. F. Ohmura, F. J. Burpo, C. J. Lescott, A. Ransil, Y. Yoon, W. C. Records and A. M. Belcher, *Nanoscale*, 2019, **11**, 1091–1101.
- 9 T. T. Ngo-Duc, J. M. Plank, G. Chen, R. E. S. Harrison, D. Morikis, H. Liu and E. D. Haberer, *Nanoscale*, 2018, **10**, 13055–13063.
- 10 X. Wang, T. Yang, X. Zhang, M. Chen and J. Wang, *Nanoscale*, 2017, **9**, 16728–16734.
- 11 S. Tom, H. E. Jin, K. Heo and S. W. Lee, *Nanoscale*, 2016, **8**, 15696–15701.
- 12 B. Neltner, B. Peddie, A. Xu, W. Doenlen, K. Durand, D. Soo Yun, S. Speakman, A. Peterson and A. Belcher, *ACS Nano*, 2010, **4**, 3227–3235.
- 13 P.-Y. Chen, X. Dang, M. T. Klug, J. Qi, N.-M. Dorval Courchesne, F. J. Burpo, N. Fang, P. T. Hammond and A. M. Belcher, *ACS Nano*, 2013, **7**, 6563–6574.
- 14 J. Hun Lee, B. Fan, T. D. Samdin, D. A. Monteiro, M. S. Desai, O. Scheideler, H.-E. Jin, S. Kim and S.-W. Lee, *ACS Nano*, 2017, **11**, 3632–3641.
- 15 R. A. Blaik, E. Lan, Y. Huang and B. Dunn, *ACS Nano*, 2015, **10**, 324–332.
- 16 A. N. Patel, A. Anne, A. Chovin, C. Demaille, E. Grelet, T. Michon and C. Taofifenua, *Small*, 2017, **13**, 1–11.
- 17 K. Torbensen, A. N. Patel, A. Anne, A. Chovin, C. Demaille, L. Bataille, T. Michon and E. Grelet, *ACS Catal.*, 2019, **9**, 5783–5796.
- 18 H. Peng and I. A. Chen, *ACS Nano*, 2019, **13**, 1244–1252.
- 19 H. Peng, R. E. Borg, A. B. N. Nguyen and I. A. Chen, *ACS Sensors*, 2020, **5**, 1491–1499.
- 20 T. Briolay, T. Petithomme, M. Fouet, N. Nguyen-Pham, C. Blanquart and N. Boisgerault, *Mol. Cancer*, 2021, **20**, 1–24.
- 21 H. Peng, R. E. Borg, L. P. Dow, B. L. Pruitt and I. A. Chen, *Proc. Natl. Acad. Sci. U. S. A.*, 2020, **117**, 1951–1961.
- 22 H. Peng and I. A. Chen, *Curr. Opin. Biotechnol.*, 2021, **68**, 23–29.
- 23 S. Y. Yoo, K. R. Shrestha, S. N. Jeong, J. I. Kang and S. W. Lee, *Nanoscale*, 2017, **9**, 17109–17117.
- 24 B. Cao, M. Yang and C. Mao, *Acc. Chem. Res.*, 2016, **49**, 1111–1120.
- 25 C. Mao, A. Liu and B. Cao, *Angew. Chemie - Int. Ed.*, 2009, **48**, 6790–6810.
- 26 K. S. Sunderland, M. Yang and C. Mao, *Angew. Chemie - Int. Ed.*, 2017, **56**, 1964–1992.
- 27 S. Shukla, H. Hu, H. Cai, S. K. Chan, C. E. Boone, V. Beiss, P. L. Chariou and N. F. Steinmetz, *Annu. Rev. Virol.*, 2020, **7**, 559–587.
- 28 K. K. Palaniappan, R. M. Ramirez, V. S. Bajaj, D. E. Wemmer, A. Pines and M. B. Francis, *Angew. Chemie - Int. Ed.*, 2013, **52**, 4849–4853.
- 29 P. E. Saw and E. W. Song, *Protein Cell*, 2019, **10**, 787–807.
- 30 A. De La Cotte, C. Wu, M. Trévisan, A. Repula and E. Grelet, *ACS Nano*, 2017, **11**, 10616–10622.
- 31 L. Ceppi, N. M. Bardhan, Y. Na, A. Siegel, N. Rajan, R. Fruscio, M. G. Del Carmen, A. M. Belcher and M. J. Birrer, *ACS Nano*, 2019, **13**, 5356–5365.
- 32 D. Ghosh, A. G. Kohli, F. Moser, D. Endy and A. M. Belcher, *ACS Synth. Biol.*, 2012, **1**, 576–582.
- 33 M. L. Embleton, S. P. Nair, W. Heywood, D. C. Menon, B. D. Cookson and M. Wilson, *Antimicrob. Agents Chemother.*, 2005, **49**, 3690–3696.
- 34 J. Rhee, M. Baksh, C. Nycholat, J. C. Paulson, H. Kitagishi and M. G. Finn, *Biomacromolecules*, 2012, **13**, 2333–2338.
- 35 B. Cao, H. Xu, M. Yang and C. Mao, in *Methods in Molecular Biology*, 2018, **1776**, 643–652.
- 36 N. Gandra, G. Abbineni, X. Qu, Y. Huai, L. Wang and C. Mao, *Small*, 2013, **9**, 215–221.
- 37 N. Stephanopoulos, G. J. Tong, S. C. Hsiao and M. B. Francis, *ACS Nano*, 2010, **4**, 6014–6020.
- 38 B. A. Cohen and M. Bergkvist, *J. Photochem. Photobiol. B Biol.*, 2013, **121**, 67–74.
- 39 S. Lin, C. Liu, X. Han, H. Zhong and C. Cheng, *Int. J. Mol. Sci.*, 2021, **22**, 1–15.
- 40 X. He, Y. Yang, Y. Guo, S. Lu, Y. Du, J. J. Li, X. Zhang, N. L. C. Leung, Z. Zhao, G. Niu, S. Yang, Z. Weng, R. T. K. Kwok, J. W. Y. Lam, G. Xie and B. Z. Tang, *J. Am. Chem. Soc.*, 2020, **142**, 3959–3969.
- 41 A. Mai-Prochnow, J. G. K. Hui, S. Kjelleberg, J. Rakonjac, D. McDougald and S. A. Rice, *FEMS Microbiol. Rev.*, 2015, **39**, 465–487.
- 42 C. M. Carmody, J. M. Goddard and S. R. Nugen, *Bioconjug. Chem.*, 2021, **32**, 466–481.
- 43 P. Passaretti, I. Khan, T. R. Dafforn and P. Goldberg Oppenheimer, *Sci. Rep.*, 2020, **10**, 18538.
- 44 B. Sampaiolese, A. Bergia, A. Scipioni, G. Zuccheri, M. Savino, B. Samori and P. De Santis, *Proc. Natl. Acad. Sci. U. S. A.*, 2002, **99**, 13566–13570.
- 45 G. Zuccheri, A. Scipioni, V. Cavaliere, G. Gargiulo, P. De Santis and B. Samori, *Proc. Natl. Acad. Sci. U. S. A.*, 2001, **98**, 3074–3079.
- 46 M. Hamzeh-Mivehroud, A. Mahmoudpour and S. Dastmalchi, *Chem. Biol. Drug Des.*, 2012, **79**, 246–259.
- 47 N. Tebbutt, M. W. Pedersen and T. G. Johns, *Nat. Rev. Cancer*, 2013, **13**, 663–673.
- 48 M. Gao, H. Su, G. Lin, S. Li, X. Yu, A. Qin, Z. Zhao, Z. Zhang and B. Z. Tang, *Nanoscale*, 2016, **8**, 15027–15032.
- 49 M. Hashemkhani, G. Demirci, A. Bayir, A. Muti, A. Sennaroglu, L. Mohammad-Hadi, E. Yaghini, M. Loizidou, S. MacRobert and H. Yagci Acar, *Nanoscale*, 2021, **13**, 14879–14899.
- 50 M. C. Lo Giudice, F. Meder, E. Polo, S. S. Thomas, K. Alnahdi, S. Lara and K. A. Dawson, *Nanoscale*, 2016, **8**, 16969–16975.
- 51 L. García-Fernández, J. García-Pardo, O. Tort, I. Prior, M. Brust, E. Casals, J. Lorenzo and V. F. Puentes, *Nanoscale*, 2017, **9**, 6111–6121.
- 52 A. Faucon, H. Benhelli-Mokrani, F. Fleury, S. Dutertre, M. Tramier, J. Boucard, L. Lartigue, S. Nedellec, P. Hulin and E. Ishow, *Nanoscale*, 2017, **9**, 18094–18106.
- 53 H. Jin, J. Pi, Y. Zhao, J. Jiang, T. Li, X. Zeng, P. Yang, C. E.

- Evans and J. Cai, *Nanoscale*, 2017, **9**, 16365–16374.
- 54 A. Khanezhari, J. C. Fraire, M. Xi, A. Feizpour, F. Xu, L. Wu, E. A. Coronado and B. M. Reinhard, *Nanoscale*, 2018, **10**, 6712–6723.
- 55 S. J. Kang, H. Y. Jeong, M. W. Kim, I. H. Jeong, M. J. Choi, Y. M. You, C. S. Im, I. H. Song, T. S. Lee and Y. S. Park, *Nanoscale*, 2018, **10**, 19338–19350.
- 56 Y. Li, Y. Du, X. Liang, T. Sun, H. Xue, J. Tian and Z. Jin, *Nanoscale*, 2018, **10**, 16738–16749.
- 57 W. J. McDaid, M. K. Greene, M. C. Johnston, E. Pollheimer, P. Smyth, K. McLaughlin, S. Van Schaeybroeck, R. M. Straubinger, D. B. Longley and C. J. Scott, *Nanoscale*, 2019, **11**, 20261–20273.
- 58 K. Li, Y. Chen, S. Li, H. G. Nguyen, Z. Niu, S. You, C. M. Mello, X. Lu and Q. Wang, *Bioconjug. Chem.*, 2010, **21**, 1369–1377.
- 59 J. M. L. Bernard and M. B. Francis, *Front. Microbiol.*, 2014, **5**, 1–7.
- 60 Z. M. Carrico, M. E. Farkas, Y. Zhou, S. C. Hsiao, J. D. Marks, H. Chokhawala, D. S. Clark and M. B. Francis, *ACS Nano*, 2012, **6**, 6675–6680.
- 61 G. Abbineni, S. Modali, B. Safiejko-Mroccka, V. A. Petrenko and C. Mao, *Mol. Pharm.*, 2010, **7**, 1629–1642.
- 62 S. Demartis, A. Obinu, E. Gavini, P. Giunchedi and G. Rassu, *Dye. Pigment.*, 2021, **188**, 109236.
- 63 N. Vanerio, M. Stijnen, B. A. J. M. De Mol and L. M. Kock, *Photobiomodulation, Photomedicine, Laser Surg.*, 2019, **37**, 383–394.
- 64 Ł. Moczek and M. Nowakowska, *Biomacromolecules*, 2007, **8**, 433–438.
- 65 M. P. Serrano, M. Rafti, A. H. Thomas and C. D. Borsarelli, *RSC Adv.*, 2019, **9**, 19226–19235.
- 66 M. Dabrzalska, N. Benseny-Cases, R. Barnadas-Rodríguez, S. Mignani, M. Zablocka, J. P. Majoral, M. Bryszewska, B. Klajnert-Maculewicz and J. Cladera, *Anal. Bioanal. Chem.*, 2016, **408**, 535–544.
- 67 A. Cantelli, F. Piro, P. Pecchini, M. Di Giosia, A. Danielli and M. Calvaresi, *J. Photochem. Photobiol. B Biol.*, 2020, **206**, 111852.
- 68 H. Ding, H. Yu, Y. Dong, R. Tian, G. Huang, D. A. Boothman, B. D. Sumer and J. Gao, *J. Control. Release*, 2011, **156**, 276–280.
- 69 A. Soldà, A. Cantelli, M. Di Giosia, M. Montalti, F. Zerbetto, S. Rapino and M. Calvaresi, *J. Mater. Chem. B*, 2017, **5**, 6608–6615.
- 70 M. Di Giosia, P. H. H. Bomans, A. Bottoni, A. Cantelli, G. Falini, P. Franchi, G. Guarracino, H. Friedrich, M. Lucarini, F. Paolucci, S. Rapino, N. A. J. M. Sommerdijk, A. Soldà, F. Valle, F. Zerbetto and M. Calvaresi, *Nanoscale*, 2018, **10**, 9908–9916.
- 71 M. Di Giosia, A. Soldà, M. Seeger, A. Cantelli, F. Arnesano, M. I. Nardella, V. Mangini, F. Valle, M. Montalti, F. Zerbetto, S. Rapino, M. Calvaresi and V. Ntziachristos, *Adv. Funct. Mater.*, 2021, **2101527**, 1–8.
- 72 A. Cantelli, M. Malferrari, A. Soldà, G. Simonetti, S. Forni, E. Toscanella, E. J. Mattioli, F. Zerbetto, A. Zanelli, M. Di Giosia, M. Zangoli, G. Barbarella, S. Rapino, F. Di Maria and M. Calvaresi, *JACS Au*, 2021, **1**, 925–935.
- 73 K. Chen, P. He, Z. Wang and B. Z. Tang, *ACS Nano*, 2021, **15**, 7735–7743.
- 74 D. K. Ji, G. Reina, S. Guo, M. Eredia, P. Samori, C. Ménard-Moyon and A. Bianco, *Nanoscale Horizons*, 2020, **5**, 1240–1249.
- 75 W. J. Chung, D. Y. Lee and S. Y. Yoo, *Int. J. Nanomedicine*, 2014, **9**, 5825–5836.
- 76 T. Urquhart, E. Daub and J. F. Honek, *Bioconjug. Chem.*, 2016, **27**, 2276–2280.
- 77 B. Oller-Salvia and J. W. Chin, *Angew. Chemie - Int. Ed.*, 2019, **58**, 10844–10848.
- 78 L. Wu, T. Huang, L. Yang, J. Pan, S. Zhu and X. Yan, *Angew. Chemie - Int. Ed.*, 2011, **50**, 5873–5877.
- 79 M. Torres-Acosta, A. González-Mora, F. Ruiz-Ruiz, M. Rito-Palomares and J. Benavides, *J. Chem. Technol. Biotechnol.*, 2020, **95**, 2822–2833.
- 80 S. Klutz, L. Holtmann, M. Lobedann and G. Schembecker, *Chem. Eng. Sci.*, 2016, **141**, 63–74.
- 81 L. Li, A. M. Belcher and D. K. Loke, *Nanoscale*, 2020, **12**, 24214–24227.
- 82 K. Ariga, *Nanoscale Horizons*, 2021, **6**, 364–378.
- 83 R. Baskaran, J. Lee and S.-G. Yang, *Biomater. Res.*, 2018, **22**, 25.